Chemical Engineering Science 139 (2016) 125–141

Contents lists available at ScienceDirect

Chemical Engineering Science

journal homepage: www.elsevier.com/locate/ces

Mixing of Newtonian and viscoelastic fluids using "butterfly" impellers

J. Ramsay [a], M.J.H. Simmons [a,*], A. Ingram [a], E.H. Stitt [b]

[a] School of Chemical Engineering, University of Birmingham, Birmingham B15 2TT, UK
[b] Johnson Matthey Technology Centre, Billingham TS23 1LB, UK

HIGHLIGHTS

- "Butterfly" impellers used for processing of viscoelastic fluids.
- Low impeller Power number *Po* due to low blade area.
- Maximum shear rates of 17 s^{-1} in region between impeller and wall at $N=60$ rpm.
- Mixing times longer in viscoelastic fluids due to elastic effects.

ARTICLE INFO

Article history:
Received 30 April 2015
Received in revised form
28 August 2015
Accepted 23 September 2015

Keywords:
Impeller
PIV
PLIF
Shear rates
Velocities
Viscoelasticity

ABSTRACT

The mixing of high viscosity and viscoelastic fluids may be performed in industry using a "butterfly" impeller, which has received scant attention. This paper describes the characterisation of these impellers using both Newtonian and viscoelastic (Boger) fluids with an identical base viscosity under laminar flow conditions in batch tanks without baffles. Measurements are made using two rotational speeds ($N=30$ or 60 rpm) over a wide range of impeller to tank diameter ratios from 0.53 to 0.98. Particle Image Velocimetry (PIV) and Planar Laser Induced Fluorescence (PLIF) have been used to determine local velocity fields, shear rates, flow numbers and mixing times, with impeller power number *Po* obtained from torque measurements. A down-pumping flow pattern is observed, with maximum normalised velocities of 25% of the impeller tip speed observed in the axial plane, increasing to 60% in the rotational plane due to solid body rotation. Angle resolved measurements found these to be slightly increased as the impeller passes the image plane, with viscoelastic fluids displaying a greater uniformity of velocity across the image planes due to elastic energy storage. Maximum shear rates are greatest between the impeller and the wall, yet remain low i.e. $O(10)\ s^{-1}$. Mixing times obtained from PLIF show that mixing times in viscoelastic fluids show a slight reduction compared to the Newtonian equivalent. The impeller power number was determined as $Po=0.6$ in the turbulent regime, while the laminar constant K_p and the Metzner–Otto constant k_s were equal to 122 and 16.0 respectively.

1. Introduction

Agitated stirred tanks have been the subject of considerable investigation in the open literature. Research has been carried out into the flows of various different fluids with both Newtonian and non-Newtonian rheology in vessels with many different impeller geometries, often with the primary aim of characterising the effectiveness of new blade designs (Ihejirika and Ein-Mozaffari, 2007; Szalai et al., 2004) and the development of scaling rules (Paul et al., 2003). The formulation of fluids with complex rheology is often carried out in a batch configuration; this includes complex multiphase products such as paints, inks and ceramic pastes which often require agitation to achieve the homogeneous dispersion of solids throughout a liquid matrix. At high solids loadings, these fluids display highly viscous or viscoelastic behaviour, and therefore mixing takes place in laminar flow. It is commonly vital to minimise or prevent the entrainment of air or other gases in order to ensure product consistency, as often it is exceedingly difficult to remove entrained gases from the viscous medium afterwards (Paul et al., 2003). An agitator often referred to as a "butterfly" impeller is often employed in batch systems for such mixing duties by manufacturers such as Westerlins (Malmö, Sweden) and VMA-Getzmann GmbH (Reichshof, Germany); an example of such a design is shown in Fig. 1 with three hollow triangular blades attached to a cylindrical hub.

* Corresponding author. Tel.: +44 121 414 5371.
E-mail address: m.j.simmons@bham.ac.uk (M.J.H. Simmons).

http://dx.doi.org/10.1016/j.ces.2015.09.026

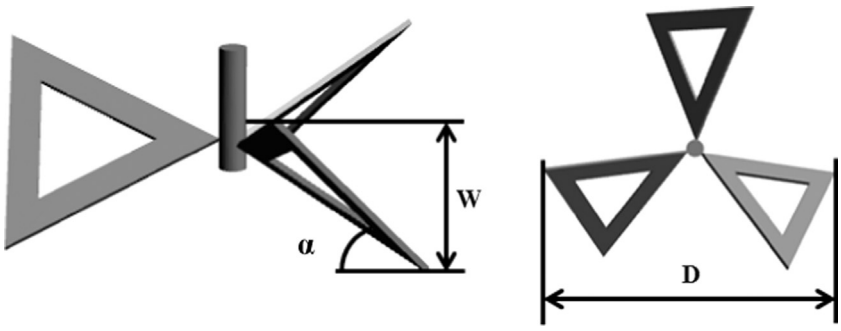

Fig. 1. Typical butterfly impeller.

Despite the myriad of impeller geometries subject to academic scrutiny there is, surprisingly, no work available describing the performance of butterfly impellers in any geometry. These impellers are thought to be advantageous by causing minimal entrainment of air during mixing, as well as the belief that they provide a uniform shear environment when operated in a close-clearance configuration, with impeller to tank diameter ratios *D/T* typically in excess of 0.9. However, much of this knowledge is based on operational experience and has minimal grounding in rigorous scientific investigation. Thus the mechanisms these impellers use to achieve mixing are poorly understood, which makes the design and optimisation of processes using these impellers difficult to implement, which has implications for process efficiency and overall product quality.

The complexity of the mixing operation is driven primarily by the highly nonlinear constitutive (viscoelastic) behaviour of the fluid products, which is a function of the polymeric liquids and multiple phases (particles, bubbles, drops) present (Paul et al., 2003). Whilst viscoelastic fluids have been the subject of much investigation over the years, beginning with Weissenberg's observation of rod-climbing phenomena (Weissenberg, 1947), there has been little in the way of investigation into their effect on processes, although stirred tank geometries are the most well developed area. The majority of previous research has focused on bulk mixing effects such as mixing times or power draw, with only a few select studies observing the fluid hydrodynamics within the fluid itself (e.g. Ozcan-Taskin and Nienow, 1995). Little research has been performed into observing flow structures or their relation to level of fluid elasticity, with Stokes' (Stokes, 1998) work into swirling flow being a notable exception. Both works characterised the elasticity through determination of the Elasticity number *El*, which Stokes found to be the controlling parameter in whether flows are elastically or inertially driven. Where flow dynamics have been investigated, most work has been performed using dye decolourisation (Lehwald et al., 2010; Shervin et al., 1991) or Particle Image Velocimetry (PIV) (Adrian, 1991; Chung et al., 2009). The fluids used in these investigations vary; however they are all optically transparent. A class of fluids called “Boger” fluids, which have a constant fluid viscosity and measurable elastic component, have been used in some studies as they allow for relatively simple separation of viscous and elastic effects (Boger and Yeow, 1992).

Despite planar laser induced fluorescence (PLIF) having been used to assess mixing in many systems (Adams and Barigou, 2007; Alberini et al., 2014; Guillard et al., 2000; Hu et al., 2010, 2012; Law and Wang, 2000; Szalai et al., 2004) the application of the technique to viscoelastic fluids is limited. Stokes and Boger (Stokes et al., 2001) studied the mixing performance of swirling flows using PLIF, highlighting the presence of different elastic regimes in a simple geometry. Further, though the calculation of mixing times using PLIF has received some attention (Busciglio et al., 2014; Hu et al., 2012; Zadghaffari et al., 2009; Zhang et al., 2013), little is available on the application of this method with viscoelastic fluids. Ozcan-Taskin and Nienow (1995) investigated flow fields and calculated mixing times for low elasticity fluids using a fibre-optic technique, additionally calculating mixing times in viscoelastic media, whilst a colorimetric method was adopted by Chhabra et al. (2007).

The application of close-clearance impeller geometries in the blending of highly viscous or viscoelastic fluids has been previously performed with both helical ribbons (Ihejirika and Ein-Mozaffari, 2007) and the Maxblend design (Fontaine et al., 2013). These geometries are almost universally employed in the blending of complex fluids, as they all possess low power draw in laminar flow. Direct torque measurement has been performed to obtain power curves in laminar flow (Fradette et al., 2007; Zhang et al., 2013; Fontaine et al., 2013), whilst flow measurements have been found using both intrusive methods such as Laser Doppler Anemometry (Jahangiri, 2007) and non-intrusive methods investigating opaque systems (Patel et al., 2014; Ihejirika and Ein-Mozaffari, 2007) and transparent varieties (Stobiac et al., 2014; Chhabra et al., 2007; Shervin et al., 1991). PIV measurements have become prevalent as the method of choice for non-intrusive determination of flow fields, owing to their non-intrusive nature and ease of application.

This work seeks to characterise the mixing of “butterfly” impellers via investigation of their mixing performance. Flow dynamics have been determined from PIV measurements, power draw and energy consumption from torque measurements and mixing times from PLIF. Their behaviour has been examined using fluids of increasing complexity using transparent Newtonian and Boger fluids with the same base viscosity. Key performance parameters such as impeller power number and pumping capacity, local shear rates and mixing times have been evaluated over a range of industrially relevant process conditions.

2. Materials and methods

2.1. Experimental set-up

Experiments were performed in an unbaffled batch stirred tank constructed from poly(methyl methacrylate) using a range of impeller diameters D between $D=80$ mm and $D=148$ mm and two rotational speeds N ($N=30$ rpm and $N=60$ rpm) at a tank diameter $T=152$ mm. The impellers were constructed of stainless steel, with three hollow triangular blades affixed to a cylindrical hub with a diameter of 18 mm. The impellers were driven by a Heidolph RZR-2102 laboratory stirrer (Heidolph UK). Other geometric parameters were kept constant, and are listed in Table 1 below. Fig. 2a and b displays the full experimental set-up. Observations made using PIV were taken in the axial (r, z) plane through the vessel diameter, and also at five rotational (r, θ) planes at

Table 1
Experimental conditions for PIV and PLIF experiments.

Impeller diameter *D* (mm)	Tank diameter *T* (mm)	Impeller off-bottom clearance *C* (mm)	Impeller blade width *W* (mm)	*D/T* (dimensionless)	*C/T* (dimensionless)	*W/D* (dimensionless)	Impeller rotation rate *N* (rpm)	Reynolds number *Re* (dimensionless)
80	152	40	64	0.53	0.26	0.80	30	20
80	152	40	64	0.53	0.26	0.80	60	39
120	152	40	96	0.79	0.26	0.80	30	45
120	152	40	96	0.79	0.26	0.80	60	88
148	152	40	119	0.98	0.26	0.80	30	68
148	152	40	119	0.98	0.26	0.80	60	134

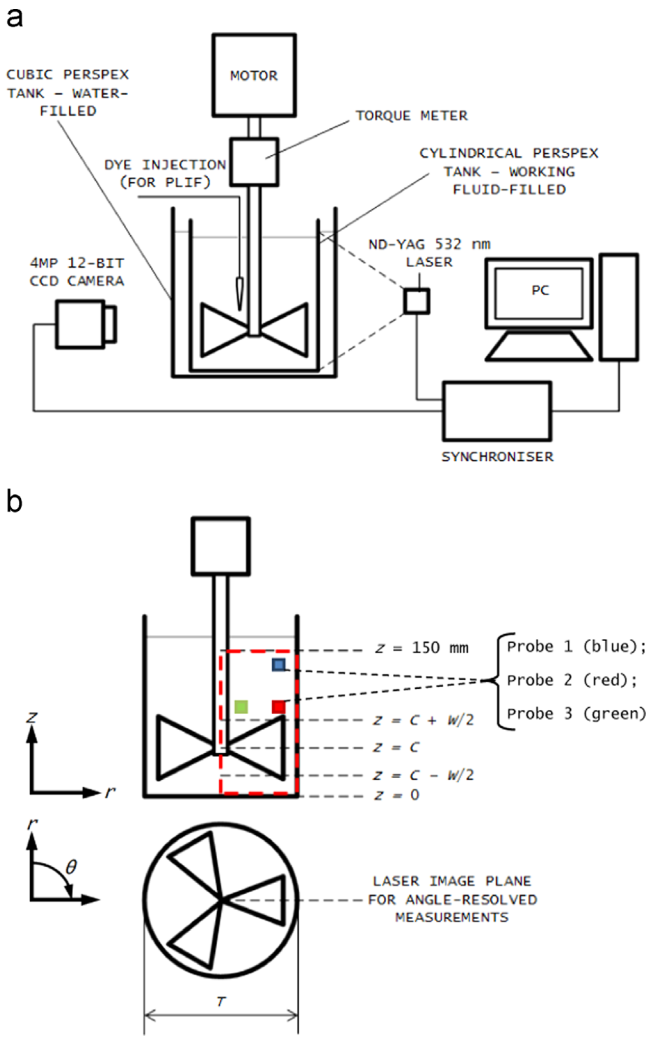

Fig. 2. (a) Experimental set-up for PIV and PLIF experiments. (b) Experimental image planes in stirred tank geometries.

constant z as shown in Fig. 2b. The range of experimental conditions selected is typical of the industrial rotational speeds and impeller-to-tank diameter D/T ratios that butterfly impellers are typically employed in. Reynolds numbers are such that flows are in the laminar and low transitional region; owing to the polymeric turbulent drag reduction and the unbaffled nature of the vessel it is expected that the laminar regime persists beyond $Re=10$, and therefore the effect of the onset of turbulence is expected to be minimal. Further, these values are based on the impeller tip speed which may provide an overestimation of Reynolds number; see Fig. 4 and the ensuing discussion for further justification.

2.2. Fluid formulation

Fluids were formulated using a bench-scale laboratory mixer. Dilute polymer solutions of polyacrylamide (Sigma Aldrich, UK) and carboxymethyl cellulose (CMC) (Sigma Aldrich, UK) in aqueous glycerol (ReAgent, UK) were formulated, with water used to make up the remainder. Sodium chloride salt was added to aid dissolution of the polymers. Boger fluid formulations were selected in order to provide viscosities and elasticities similar to a range of industrially relevant viscoelastic materials. Rheological characterisation was performed using a Discovery Hybrid HR-2 and an AR-2000 rheometer (TA Instruments, USA) using a 40 mm 4° cone and plate geometry over the range of shear rates $\dot{\gamma}$ between 0.1 and 100 s^{-1}. This shear rate range was selected as an approximation of the tank-averaged shear rate using the Metzner–Otto correlation ($\dot{\gamma}=k_sN$) found the value to be 11.5 s^{-1} for a down-pumping pitched blade turbine (PBTd), which as an initial approximation is within the measured range. Normal stress differences N_1, which are viscometric material properties arising as a result of differences in normal components of the stress tensor (Phan-Thien, 2002), were obtained during the acquisition of shear stress versus shear rate data on the same instrument through axial force measurement.

Relaxation times were then calculated from normal stress difference data and values were fitted to a power law model (Ozcan-Taskin, 1993) such that:

$$\lambda=\frac{\psi_1(\dot{\gamma})}{2\eta(\dot{\gamma})}=\frac{1}{2\eta(\dot{\gamma})}\left(\frac{N_1(\dot{\gamma})}{\dot{\gamma}^2}\right) \tag{1}$$

$$\lambda=a\dot{\gamma}^b \tag{2}$$

where ψ_1 is the first normal stress coefficient, η the fluid apparent viscosity, N_1 the first normal stress difference, $\dot{\gamma}$ the shear rate, while a and b are constants. The compositions of the model fluids used and their rheological parameters can be found in Table 2. Fig. 3a and b displays the rheological data obtained.

As Fig. 3a shows, both Boger fluids possess similar viscosities, indicating that glycerol concentration controls overall solution viscosity and thus allows investigation of the varying elasticities of each fluid independently. These elastic responses are shown in Fig. 3b: the outlined symbols show the response of first normal stress difference N_1 with shear rate whilst the filled symbols display the relaxation time. For both materials N_1 increases with increasing shear rate, however the rate of increase decreases at higher shear rates, indicating that the expected quadratic response of a "true" Boger fluid is only valid at low values of $\dot{\gamma}$. However, it can be seen that over the whole measured range, Boger A displays lower values of N_1, and thus lower levels of elasticity. This is also observed in the relaxation time, λ, trends. Furthermore, it can be seen that the relaxation time follows the expected trend of a power law model, as such fitting parameters are shown in Table 2. Note that normal stress measurement is highly sensitive, and as such the fitting parameters possess large standard deviations.

Table 2
Fluid compositions and rheological parameters.

		Glycerol		Boger A	Boger B
Polyacrylamide (wt%)		–		0.01	0.02
Glycerol (wt%)		90.00		90.00	90.00
Water (wt%)		10.00		8.33	8.32
Sodium chloride (wt%)		–		1.66	1.66
Fluid	**Viscosity η (Pa s)**	**Consistency index *K* (Pa s^n)**	**Viscosity power law exponent *n***	**Relaxation time pre-exponential factor *a* (s^{b+1})**	**Relaxation time power law exponent *b* (dimensionless)**
Glycerol	0.188 (±0.014)	–	–	–	–
Water	0.001 (±0.001)	–	–	–	–
12,500 cSt silicone oil	12.800 (±0.002)	–	–	–	–
4% Carboxy(methyl cellulose) in water	–	3.05 (±0.01)	0.84 (±0.01)	–	–
Boger A	0.195 (±0.019)			87.76 (±18.49)	−1.81 (±0.02)
Boger B	0.164 (±0.024)			157.36 (±31.12)	−1.78 (±0.04)

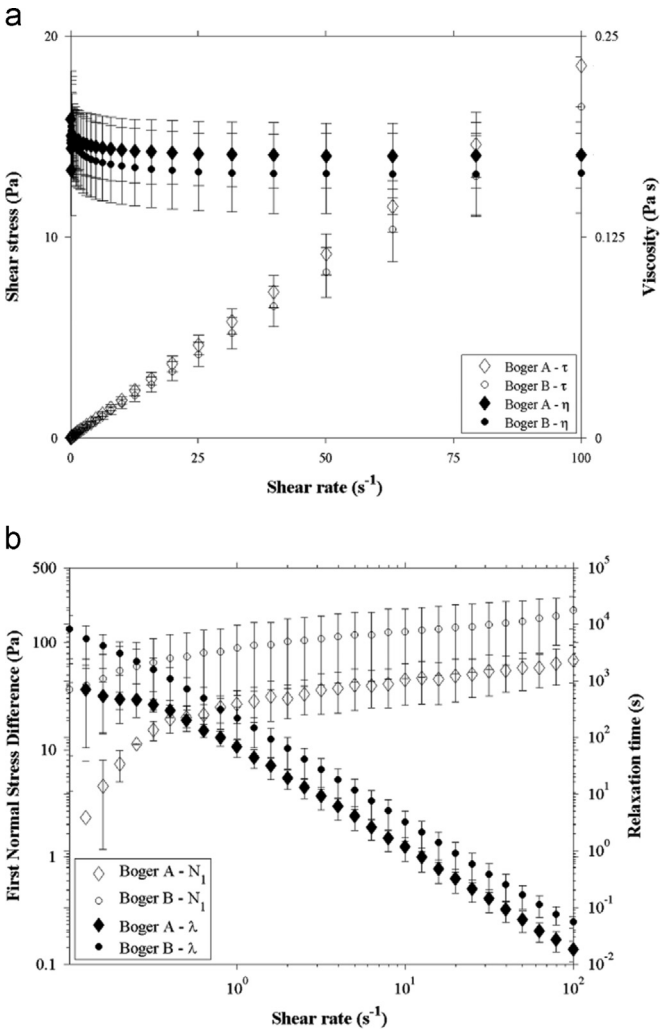

Fig. 3. (a) Shear stress τ and viscosity η versus shear rate for Boger fluids. (b) First normal stress differences N_1 and relaxation times λ for Boger fluids.

At the experimental conditions used for PIV and PLIF, experimental Reynolds numbers *Re* are laminar and vary between 20 and 134, as defined by

$$Re = \frac{\rho N D^2}{\eta} \tag{3}$$

where ρ is the fluid density.

2.3. Power curve determination

Power number curves were determined through direct torque measurement from the impeller shaft. Power draw is related to torque through the relationship:

$$P = 2\pi NM \tag{4}$$

where *P* is power, *N* is impeller rotational speed and *M* the torque on the impeller shaft. Additionally, power can be determined through assessment of the drag caused by the fluid using the impeller power number:

$$P = \rho Po N^3 D^5 \tag{5}$$

where ρ is the fluid density and *Po* the impeller Power number, a form of drag coefficient. Equating (4) and (5) allows for calculation of Power number from direct torque measurement. An optical TorqSense RWT-420 (Sensor Technology, UK) sensor was attached to the impeller shaft which was driven by a Heidolph RZR-2120 laboratory stirrer motor (Heidolph, UK). Data was acquired and analysed using TorqView software (Sensor Technology, UK).

Measurements were taken over a range of impeller speeds using different Newtonian and shear-thinning fluids enabling coverage of the laminar, transitional and turbulent flow regimes ($0.4 < Re < 50{,}000$). Water, glycerol, 12,500 cSt silicone oil and a shear-thinning solution of aqueous carboxymethyl cellulose were used, with torque data linearised and plotted graphically in order to determine the parameters *Po*, laminar gradient $K_p = Re \cdot Po$ and Metzner–Otto constant k_s respectively according to the method described in Rodgers et al. (2009). The systematic torque M_0 was also directly measured in a fluid-free system to determine the veracity of the curve fit, with a good degree of agreement found. Determination of the power number curve for a standard six-blade Rushton disc turbine (RDT) in a baffled vessel was also performed across all flow regimes to provide a comparison using a known geometry.

2.4. Particle image velocimetry (PIV)

PIV was performed on all stirred tank geometries (Table 1) using both vertical (*r*, *z*) and horizontal (*r*,θ) imaging planes as shown in Fig. 2a and b, thus the co-ordinate *r* is shared by both planes. A 532 nm Nd-YAG laser (nanoPIV, Litron, UK) operating at 7.25 Hz illuminated the stirred vessel perpendicular to the image plane. A 12-bit 4 MP CCD camera (TSI, USA) captured images synchronous to the laser pulses, with timing controlled by a synchroniser (TSI 610035) linked to a personal computer operating Insight 4 G software (TSI, USA). Rotational planes were captured by

means of a 45° mirror placed beneath the vessel, with the camera capturing the projected image. Neutrally buoyant silvered glass spheres of 10 μm diameter (Dantec Ltd., UK) were utilised within the flow. A laser sheet with a thickness less than 0.5 mm at the focal distance of the focussing lens used (500 mm) was employed to illuminate the observation plane, with the brightest portion of the sheet (at the focal distance) aligned with the centre of the field of view. The impeller blades and shaft were painted with a matte black coating to eliminate laser light reflections from surfaces. 500 image pairs were obtained for each experimental condition. The data were analysed as an ensemble and by separating successive images to obtain flow fields resolved by the position of the blade (angle-resolved). Flow fields were obtained using a recursive Nyquist grid, with initial and final interrogation areas of 64×64 pixels and 32×32 pixels respectively, with a resolution of 55 μm pixel^{-1} used for each image. The time between each laser pulse ΔT was set to 1200 μs; this value was selected in order to observe the fastest moving particles in the flow moving no more than one quarter of an interrogation region, based on a maximum rotational speed of 60 rpm and a corresponding impeller tip speed of 0.46 m s^{-1}, i.e. the largest possible velocity in any flow in this study. Additionally, this value of ΔT was sufficiently low to ensure that particles did not move out of the image plane during capture. PIV measurements have previously been found to give velocities accurate to 1–2% of the maximum (Adrian, 1991). Plots were generated from bespoke MATLAB code, with local spatial gradients being determined using a central difference method. All velocity data are displayed in a normalised form, with local velocities u shown as a fraction of impeller tip speed u_t.

PIV data was used to determine impeller pumping number N_Q:

$$N_Q = \frac{Q}{ND^3} \tag{6}$$

where Q is the impeller pumping capacity calculated from velocity data using the standard approaches described and used by Gabriele et al. (2009), amongst others. N_Q is a measure of the effectiveness of the impeller at circulating fluid within its vessel, and thus allows for comparison between different process conditions and impeller types. The flow rate from the impeller was split into two components, the axial flow $N_{Q,z}$ and the radial component $N_{Q,r}$. These were calculated from

$$Q = Q_z + Q_r \tag{7}$$

$$Q_z = \int_{\theta=0}^{\theta=2\pi} \int_{r=0}^{r=\frac{D}{2}} \left((v \cdot r)|_{z=C-\frac{W}{2}} \right) dr\, d\theta \tag{7a}$$

$$Q_r = \int_{\theta=0}^{\theta=2\pi} \int_{z=C-\frac{W}{2}}^{z=C+\frac{W}{2}} \left(u|_{r=\frac{D}{2}} \right) dz\, d\theta \tag{7b}$$

Time-averaged PIV data was used for this analysis, as this automatically provides the integral across all impeller angular positions θ. The remaining integral was calculated using bespoke MATLAB code using the trapezium rule, owing to the equal spacing of PIV velocity data after data post-processing. This provides a minimum of 42 individual velocity measurements in for the determination of Q_z and 68 data points for calculating Q_r. The ratio of radial and axial pumping numbers, $N_{Q,r}/N_{Q,z}$, was calculated to provide an assessment of impeller pumping type, i.e. radial flow, axial flow or mixed flow. The integral limits, i.e. the geometrical extent of the impeller cross-section through the flow, was selected in accordance with standard procedures assuming that the impeller sweeps a cylindrical surface during rotation.

Shear rates have been calculated using time-averaged velocity fields according to Bird et al. (1960):

$$\dot{\gamma} = \sqrt{-\mathbf{\Pi}} \tag{8}$$

$$-\mathbf{\Pi} = \left[2\left[\left(\frac{\partial v_x}{\partial x}\right)^2 + \left(\frac{\partial v_y}{\partial y}\right)^2 + \left(\frac{\partial v_z}{\partial z}\right)^2 \right] + \left[\frac{\partial v_y}{\partial x} + \frac{\partial v_x}{\partial y}\right]^2 + \left[\frac{\partial v_z}{\partial y} + \frac{\partial v_y}{\partial z}\right]^2 + \left[\frac{\partial v_x}{\partial z} + \frac{\partial v_z}{\partial x}\right]^2 \right] \tag{8a}$$

$$-\mathbf{\Pi} = \left[2\left[\left(\frac{\partial v_r}{\partial r}\right)^2 + \left(\frac{1}{r}\frac{\partial v_\theta}{\partial \theta} + \frac{v_r}{r}\right)^2 + \left(\frac{\partial v_z}{\partial z}\right)^2 \right] + \left[r\frac{\partial}{\partial r}\left(\frac{v_\theta}{r}\right) + \frac{1}{r}\frac{\partial v_r}{\partial \theta}\right]^2 + \left[\frac{1}{r}\frac{\partial v_z}{\partial \theta} + \frac{\partial v_\theta}{\partial z}\right]^2 + \left[\frac{\partial v_r}{\partial z} + \frac{\partial v_z}{\partial r}\right]^2 \right] \tag{8b}$$

where v is the velocity and subscripts x, y and z represent the principle axes in Cartesian co-ordinates whilst r, z and θ represent the radial, axial and rotational components of the flow respectively in cylindrical co-ordinates. Owing to the two-dimensional nature of PIV data acquisition, several components of the overall shear rate cannot be directly calculated from the two image planes separately. The missing components have been neglected based on the assumption of uniformity of rotational velocity gradients in the r–z plane, and negligible axial gradients in the r–θ plane. As the laser light sheet possesses a narrow thickness compared to the size of the PIV interrogation cell for data processing, it is assumed that the through-the-plane velocity components are uniform across the whole image and thus any spatial gradients are negligible.

Additionally, these shear rates can then be coupled to the local relaxation times, providing a map of local Weissenberg number magnitude which ratio of timescales of material and process deformation timescales, as described by

$$Wi = \lambda\dot{\gamma} \tag{9}$$

where Wi is the Weissenberg number and λ the fluid relaxation time. Wi has been determined both locally and as a tank average using a Metzner–Otto relationship $\dot{\gamma} = k_s N$ (Ozcan-Taskin and Nienow, 1995). The Weissenberg number can also be used to determine bulk elastic effects and to elucidate different elasticity regimes within process geometries. This is achieved through the Elasticity number, El:

$$El = \frac{Wi}{Re} \tag{10}$$

Owing to the difficulty of selecting an appropriate length scale for determining local Reynolds numbers, tank-averaged Weissenberg and Reynolds numbers have been implemented to determine average elasticity numbers.

2.5. Planar laser-induced fluorescence (PLIF)

PLIF was implemented using the same apparatus as PIV using the vertical imaging plane only with Rhodamine 6G (Sigma Aldrich, UK) as the fluorescent tracer added. Images were captured at a rate 0.5 Hz. A 545 nm cut-off filter lens was added to the camera in order to eliminate all but the light emitted by the fluorescing dye (λ=560 nm). Mixing times for the D/T=0.98 condition were calculated from the logarithm of the local concentration variance (Brown et al., 2004):

$$\log\, \sigma(\theta)^2 = \log\left(\frac{1}{1-n} \sum_{i=0}^{n} \left(C'_{a,i}(\theta) - 1 \right)^2 \right) \tag{11}$$

where σ is the concentration variance, θ is the current time, n is the maximum number of data points (in this case the total number of locations), and $C'_{a,i}$ is defined as

$$C'_{a,i} = \frac{C_{a,i} - C_0}{C_\infty - C_0} \tag{12}$$

where $C_{a,i}$' is the normalised concentration of component a at location i, $C_{a,i}$ is the concentration at location i, and the subscripts 0 and ∞ indicate the initial and fully-mixed conditions respectively (Grenville and Tilton, 1996). 90% and 95% confidence values were selected to determine final mixing time θ_M, corresponding to values of $\log \sigma^2$ of -2.0 and -2.6 respectively. Three separate virtual probe locations were utilised during image analysis in order to determine final mixing time, each probe consisting of 40 (20×20) pixels; these are shown in Fig. 2b. A calibration of the local greyscale value to dye concentration was performed to ensure all recorded greyscale values were linearly related to concentration; see Hall et al. (2005) for further details. Raw data images were pre-processed to eliminate the effect of diminishing laser light intensity across the geometry using a pixel-by-pixel calibration and then analysed using a bespoke MATLAB code.

In order to compare performance of "butterfly" impellers to other geometries, the use of theoretical mixing time correlations have been implemented. The dimensionless mixing time $N\theta_{95}$ has been evaluated for all conditions, as it has been observed that this value is constant for turbine-type impellers in Newtonian fluids in laminar flow (Grenville and Nienow, 2004).

3. Results

3.1. Power draw measurements

The constructed Reynolds number *Re* versus Power number *Po* graph is displayed in Fig. 4. Error bars display the standard deviation of the power draw at the given Reynolds number.

The linear trend observed in the laminar regime continues into the transitional region, as observed in other unbaffled vessels due to the presence of solid body rotation, thus supporting the earlier postulate that the laminar region can be assumed to continue at Reynolds numbers $Re > 10$. The values of *Po* for the RDT show good agreement with literature data (Paul et al., 2003), providing confidence in the accuracy of the torque sensor method. The "butterfly" impeller possesses a turbulent Power number of 0.6; this value is consistent with the trends reported for other unbaffled systems (Hall et al., 2004).

Table 3 displays the experimental impeller characteristics derived from the torque measurements, with data for the RDT and values for a similar conventional down-pumping pitched blade turbine (PBTd) from literature (Hall, 2005) included for comparison.

Comparing the values with that expected of a similar impeller such as a PBTd, the value of turbulent *Po* is noticeably lower ($Po \sim 0.8$ for a PBTd). This can be attributed to the minimal cross-section of the "butterfly" impeller through the flow due to the large hollow within the blade, reducing the value of *Po* in the turbulent regime. The laminar gradient K_p is greater than that of a RDT, indicating increased energy efficiency in the laminar regime. The value for a butterfly impeller is similar to that of a Maxblend impeller, albeit slightly lower due the butterfly geometry's low surface area, indicating suitability for application in viscous media. The calculated impeller Metzner–Otto constant ks is slightly higher than that expected of a pitched-blade design; however is of a similar magnitude to RDT and PBT geometries and significantly lower than those of close-clearance impellers such as anchors and helical ribbons (Paul et al., 2003). Additionally, it can be noted that the data presented are for all the impeller diameters listed in Table 1, and can be seen to collapse onto one master curve. This is consistent with previous work showing Power number to be a weak function of impeller-to-tank diameter *D*/*T* ratio (Harnby et al., 1992).

3.2. Flow hydrodynamics

3.2.1. Effect of impeller to tank diameter ratio (D/T)

The time-averaged velocity fields within the glycerol system in the axial plane as a function of *D*/*T* are shown in Fig. 5. Owing to the laminar flow, similarity in the shape of flow structures was observed in flow fields normalised by the impeller tip speed obtained at different rotational rates. Thus, unless otherwise stated, the figures represent data obtained at $N = 60$ rpm and are time-averaged. Additionally, all impeller positions marked on are virtual, i.e. they are there to indicate to position of the impeller as a whole in the flow due to the large blade hollow affecting visibility within the data images. All images display the velocity magnitude in the image plane only (i.e. u_{rz} or $u_{r\theta}$ for axial and

Table 3
Impeller performance parameters.

Impeller	Turbulent Power number *Po* (dimensionless)	Laminar Power gradient K_p (dimensionless)	Impeller Metzner–Otto constant k_s (dimensionless)
"Butterfly"	0.6	122	16.0
RDT, baffled	4.9	71	12.3
PBTd (Hall, 2005)	0.8	–[a]	11.0
Maxblend (Fradette et al., 2007)	–[a]	165	27.0

[a] The values were not reported in the comparison study.

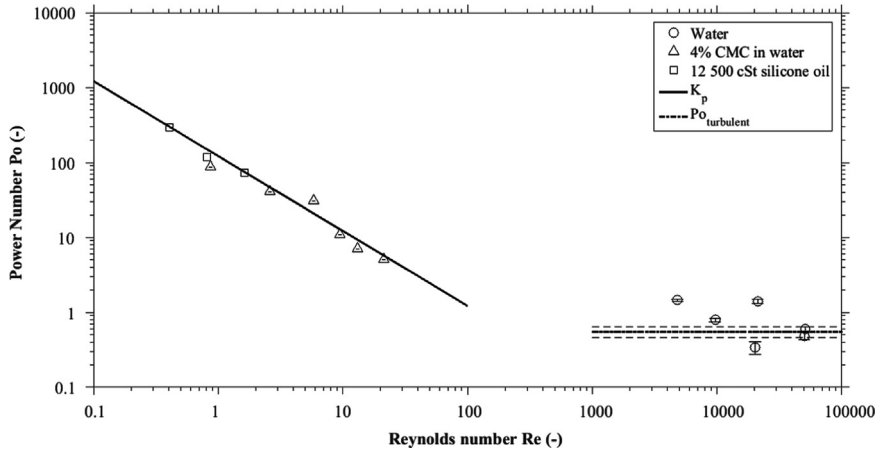

Fig. 4. Reynolds number Re versus Power number *Po* for "butterfly" impellers.

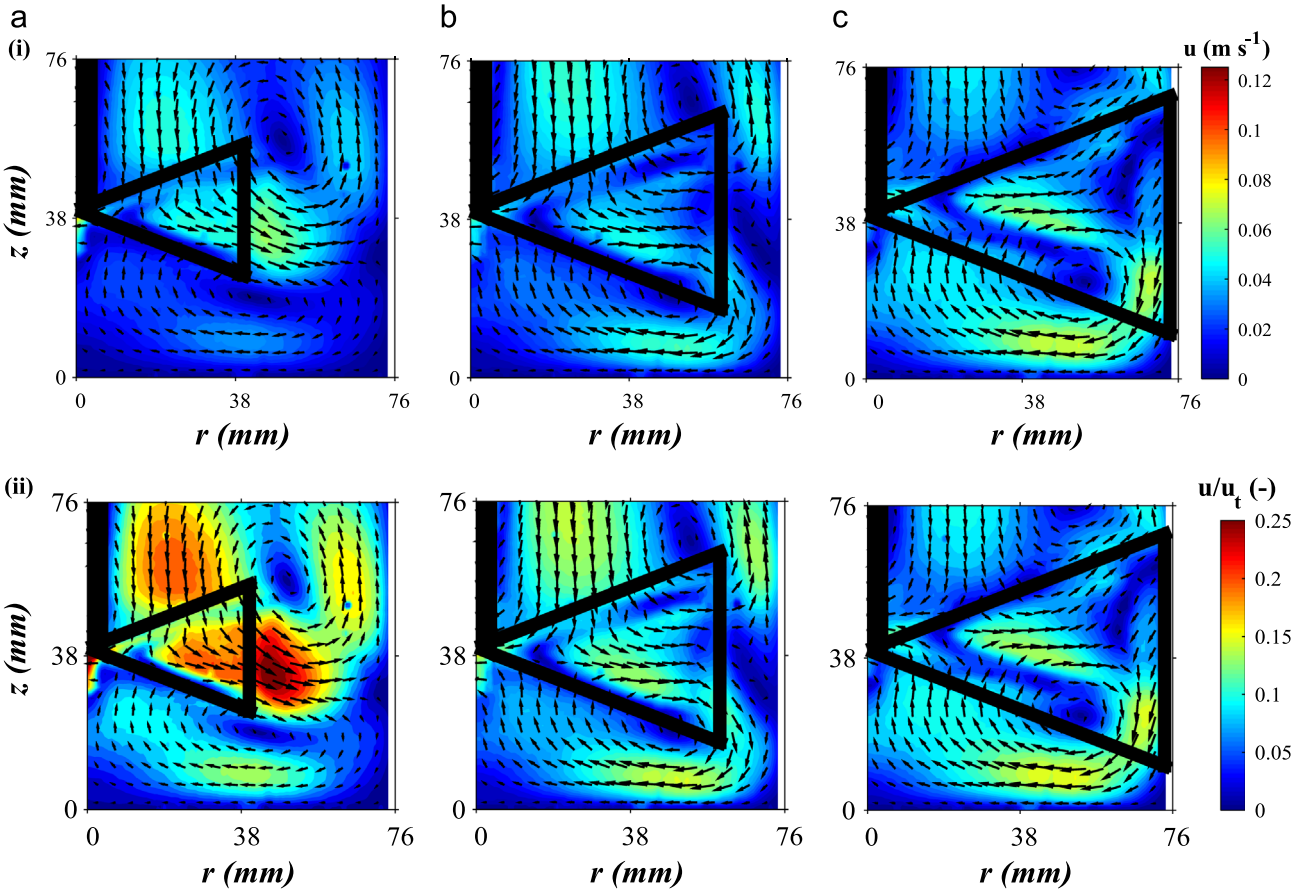

Fig. 5. Velocity plots for glycerol, T=152 mm, N=60 rpm for (a) D/T=0.53, (b) D/T=0.79, (c) D/T=0.98; (i) velocity magnitude u, (ii) normalised velocity u/u_t.

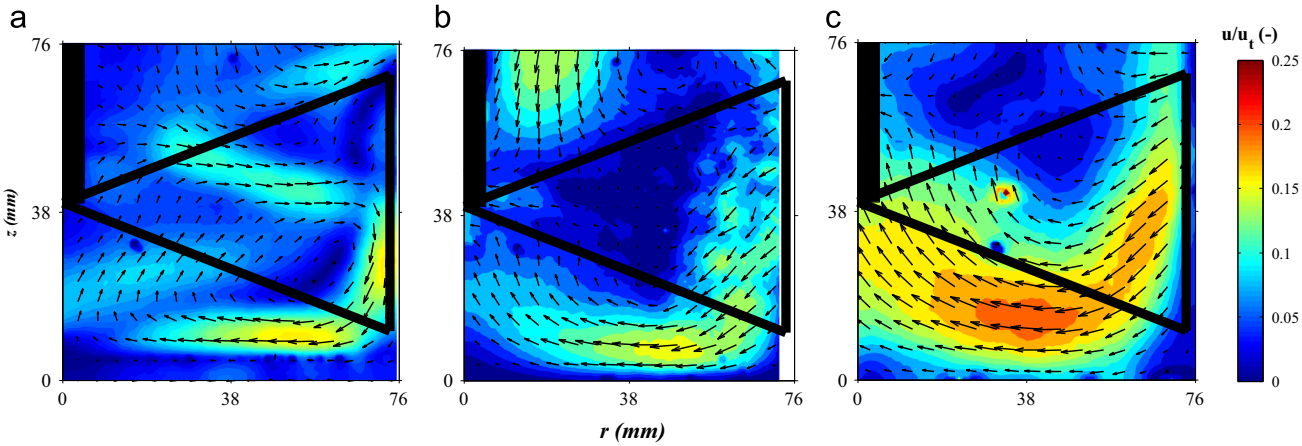

Fig. 6. Normalised velocities u/u_t, D/T=0.98; Left to right – (a) Glycerol, (b) Boger A, and (c) Boger B.

rotational sections respectively) due to the two-dimensional nature of PIV data acquisition.

At the lowest D/T ratio, a clear down-pumping flow pattern can be observed. As the upper tip of the impeller constitutes the leading edge of the blade, this pattern is consistent with the impeller blade pitch and direction of rotation. It can also be observed that immediately adjacent to the impeller blade there is a region of very low velocity indicating a very low level of radial pumping. In addition, the greatest velocities can be seen at the upper and lower impeller blade edges. Also, the impeller appears to make a significant contribution to the velocity in this plane, with large velocities observed.

As can be seen, as the value of D/T approaches unity, the bulk flow discharged by the impeller becomes increasingly confined by the wall and as such bulk fluid velocity magnitudes decrease. This phenomenon has been observed in other unbaffled geometries (Hall, 2005), owing to the dominance of solid body rotation in the impeller region within these flows. However, "butterfly" impellers are typically used operationally at close wall clearances, i.e. $D/T > 0.9$. Therefore, this study shall hereafter focus on results obtained in the D/T=0.98 geometry (also referred to as the close-clearance scenario), as this is typical of the industrial scenario and therefore of greatest relevance to this study.

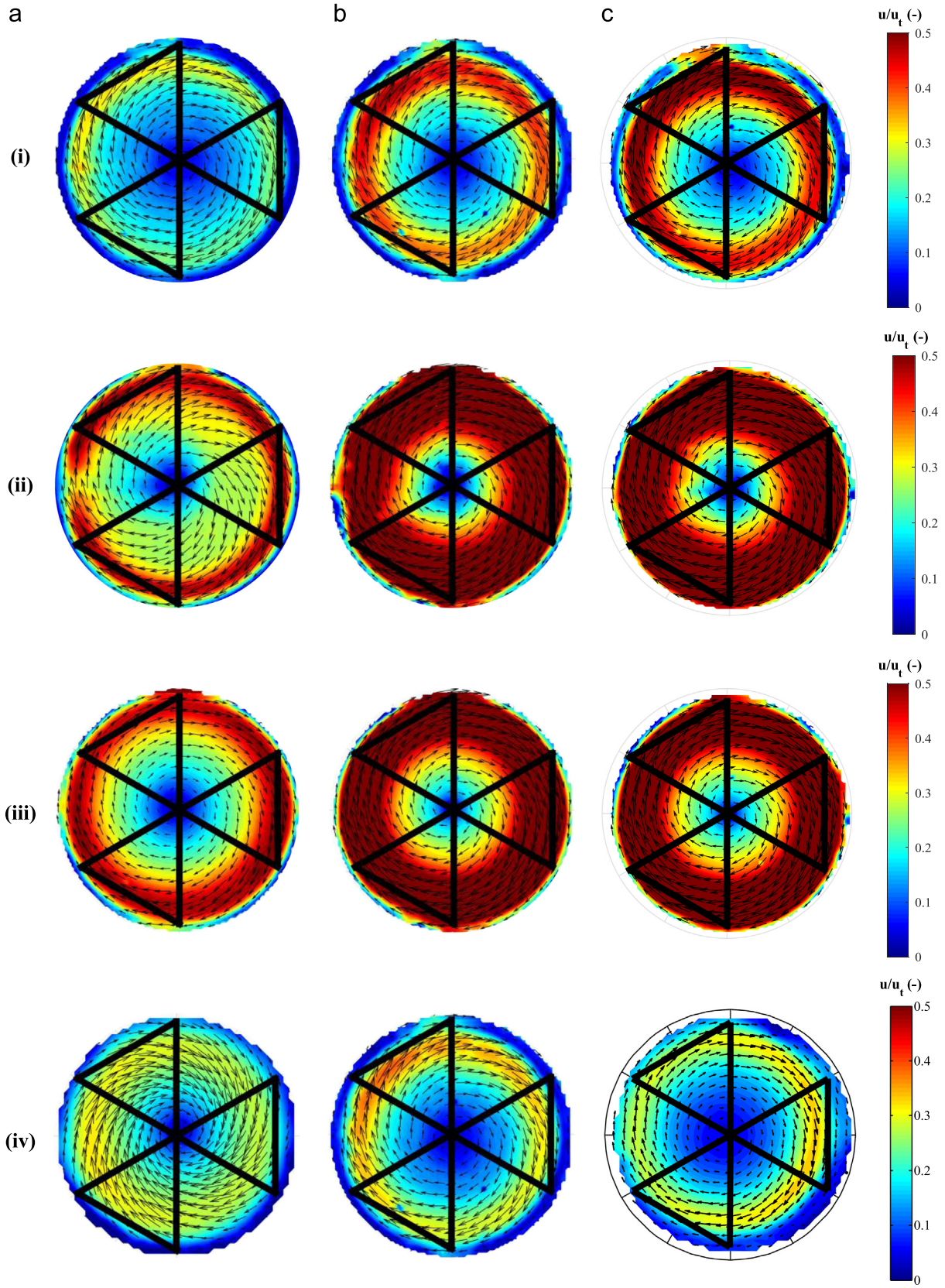

Fig. 7. Normalised velocity u/u_t, $D/T=0.98$; (a) Glycerol, (b) Boger A, (c) Boger B; (i) $z=C+W/2$, (ii) $z=C$, (iii) $z=C-W/2$, and (iv) $z=0$ mm.

3.2.2. *Effect of fluid rheology*

The time-averaged normalised velocity fields for the fluids Glycerol, Boger A and Boger B are shown in the axial plane in Fig. 6, with rotational planes shown in Fig. 7 taken at the image planes indicated in Fig. 2b. Please note the difference in colour scales between these figures; these have been selected for clarity based on the maximum normalised velocity within the image plane. Additionally, the rotational sections do not include any transects taken at $z=150$ mm

owing to exceptionally low observed velocities (< 1% of the impeller tip speed).

Fig. 6 displays significant variation in the axial velocities observed in viscoelastic fluids compared to the Newtonian equivalent. Primarily, the observed normalised velocities in the Boger fluids are measurably greater than in glycerol at the same viscosity, with maximum velocities of the order of 10% of the impeller tip speed in the bulk glycerol within the impeller the blade hollow compared to 25% in fluid Boger B. In addition, it can be seen that the direction of discharge from the impeller has shifted. Whereas in the Newtonian situation flow loops are present above and below the impeller, in the viscoelastic fluids the discharge appears to have a minimised upper flow loop. Additionally it can be seen that immediately adjacent to the impeller blade at the vessel wall, the Newtonian case exhibits a marked change in fluid direction from following the vessel radius to immediately upwards or downwards. This is contrasted with the two viscoelastic fluids, which show a relatively gentle change in direction at the wall. This behaviour can be attributed to two phenomena: the unbaffled nature of the vessel and the presence of an elastic component within the fluid. The former has been shown to significantly affect flow fields, with weak radial discharges observed from axial flow impellers in turbulent regimes (Hall et al., 2005) leading to a diminished fluid response in the axial plane. Elastic forces are known to generate normal stress differences, which induce secondary flows, thereby creating competition between themselves and the primary flow structures induced by the impeller, causing the change of pumping at the wall. This has significant implications for fluid drawdown in industrial situations, as the presence of an elastic component inhibits the impeller's ability to capture material at the fluid surface. This change of pumping type behaviour has not been previously observed in viscoelastic fluids (Ozcan-Taskin and Nienow, 1995; Seyssiecq et al., 2003), and may be attributed to narrow range of impeller D/T values previously investigated in these systems.

In addition to this, several flow effects differ in the viscoelastic fluid experiments. An ellipsoidal region of higher fluid velocity exists immediately beneath the impeller region at the centre of the downward flow loop in Fig. 6, and this displays a close to homogeneous local velocity. This indicates that there is a region of solid-like behaviour beneath the impeller, wherein the fluid behaves as one mass held together by elastic forces. Mixing in this region is expected to be limited to material already within this zone, with little material transfer outside of this zone, as shall be displayed in PLIF results in Section 4.3.

Fluid motion in the rotational direction displays the typical flow field of a rotating fluid as shown in Fig. 7. The velocity magnitude is greatest at the centre of the rotational section in each plane, i.e. midway between the impeller shaft ($r=0$ mm) and the vessel wall ($r=D/2$ mm). Radial velocity components have been found to match those found in axial plane measurements, indicating that the increase in observed velocity in this region is due to the rotational velocity component. The region of greatest normalised velocity is found directly beneath the impeller in the Newtonian system, while it is found in the centre of the impeller (i.e. at a height from the vessel base equal to the impeller clearance C) in the viscoelastic systems. This change is due to the aforementioned shift from axial to radial impeller discharge.

It is known that viscoelastic fluids, due to their relaxation time, display a time dependence that may not be visible in a time-averaged flow field. It is known that instantaneous velocities and shear rates can be greater than the average of the field, and as such must be investigated. Therefore it is prudent to observe the angle-resolved data in parallel with time-averaged data, as illustrated in Figs. 8 and 9. All angle-resolved data is shown at position $\theta=0°$ relative to the impeller, as shown in Fig. 2b.

Notable differences shown in Fig. 8 include a reduction in the recorded velocities in the axial plane for glycerol compared with both Boger fluids. This can be attributed to the maximum energy being imparted to the fluid during the passage of the impeller blade, as in viscoelastic media some of this energy is stored due to the fluid elasticity, while Newtonian fluids display no such behaviour. This is also why the viscoelastic fluids display a greater homogeneity of local velocity magnitude, resulting in fluid motion of elements agitated while the impeller was not in the plane of the image, thus resulting in a more uniform velocity field.

Rotational velocity measurements display significant variations between the Newtonian and viscoelastic cases (Fig. 9). Whereas the local velocity maxima are concentrated around the location of the impeller blades in glycerol, there is a greater uniformity across each transect with Boger fluids A and B. This can be attributed to the effect of fluid elastic energy storage allowing for greater fluid motion after the impeller blade has passed, increasing the amount of agitation the fluid receives. In addition, the effects of solid body rotation are much more pronounced in viscoelastic media, with radial velocity variation reducing as the magnitude of the fluid's elasticity increases.

Fig. 10 displays normalised velocity transects at different axial positions for the three fluids studied. It can be seen that there is significant deviation from the Newtonian case in at all positions, with this behaviour particularly pronounced in angle-resolved measurements. The increase in velocity as r/R approaches unity is significantly lower in time-averaged data, though still visible in a small peak around $r/R=0.9$. The shift in the position of the maxima is most evident in angle-resolved data, with a large increase in the local normalised velocity at $z=C-W/2$ and $z=C$ for the Boger

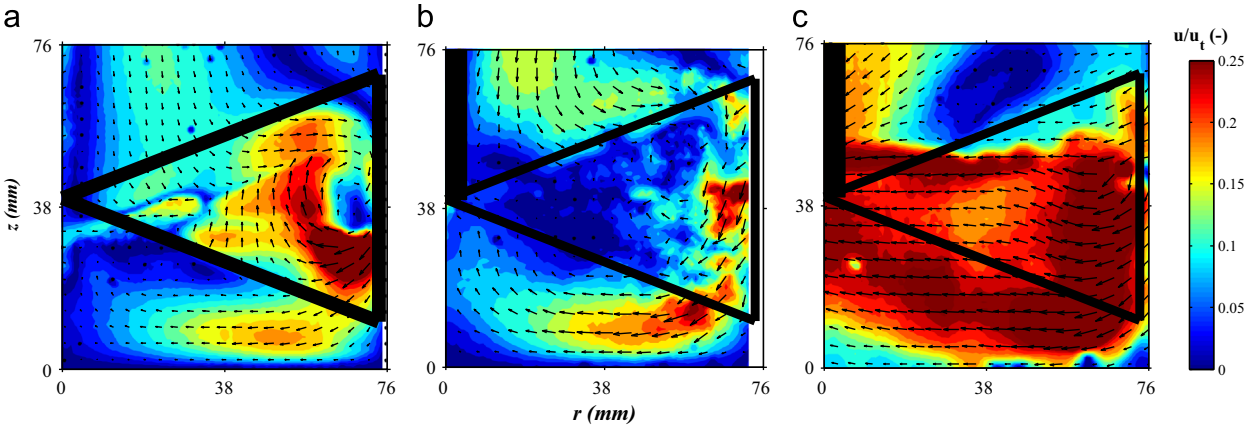

Fig. 8. Angle-resolved normalised velocity u/u_t, $D/T=0.98$; (a) Glycerol, (b) Boger A, and (c) Boger B.

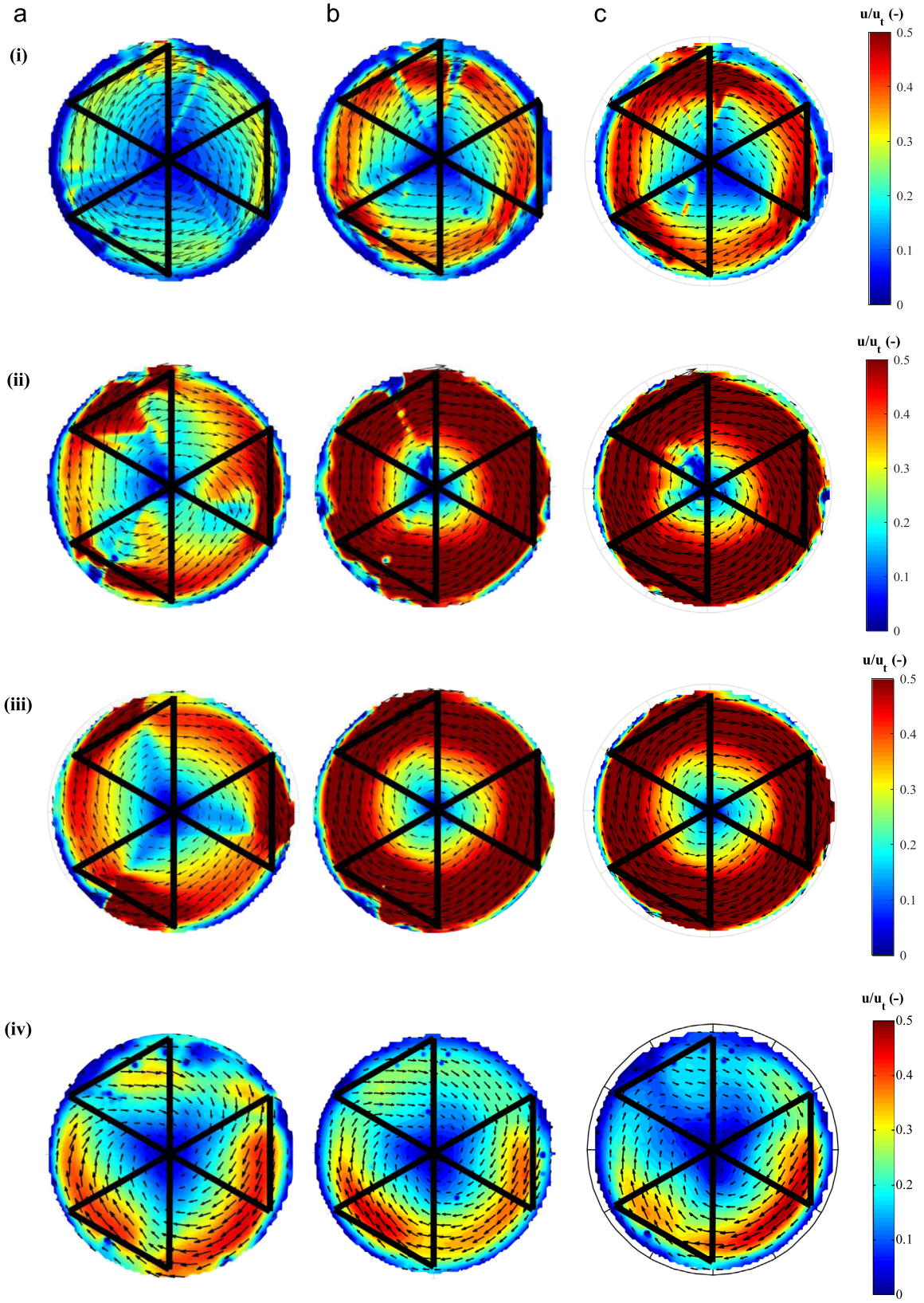

Fig. 9. Angle-resolved normalised velocity u/u_t, $D/T=0.98$; (a) Glycerol, (b) Boger A, (c) Boger B; (i) $z=C+W/2$, (ii) $z=C$, (iii) $z=C-W/2$, (iv) $z=0$ mm.

fluids, further corroborating the shift in change in impeller discharge type. It can also be observed that for all angle-resolved measurements, the local velocities displayed by Boger B are greater than those for Boger A. The increase is also seen in time averaged measurements but not to the same extent, indicating that during the impeller passage local velocities are greater in the more elastic fluid, which is consistent with the increased energy storage capacity these materials display.

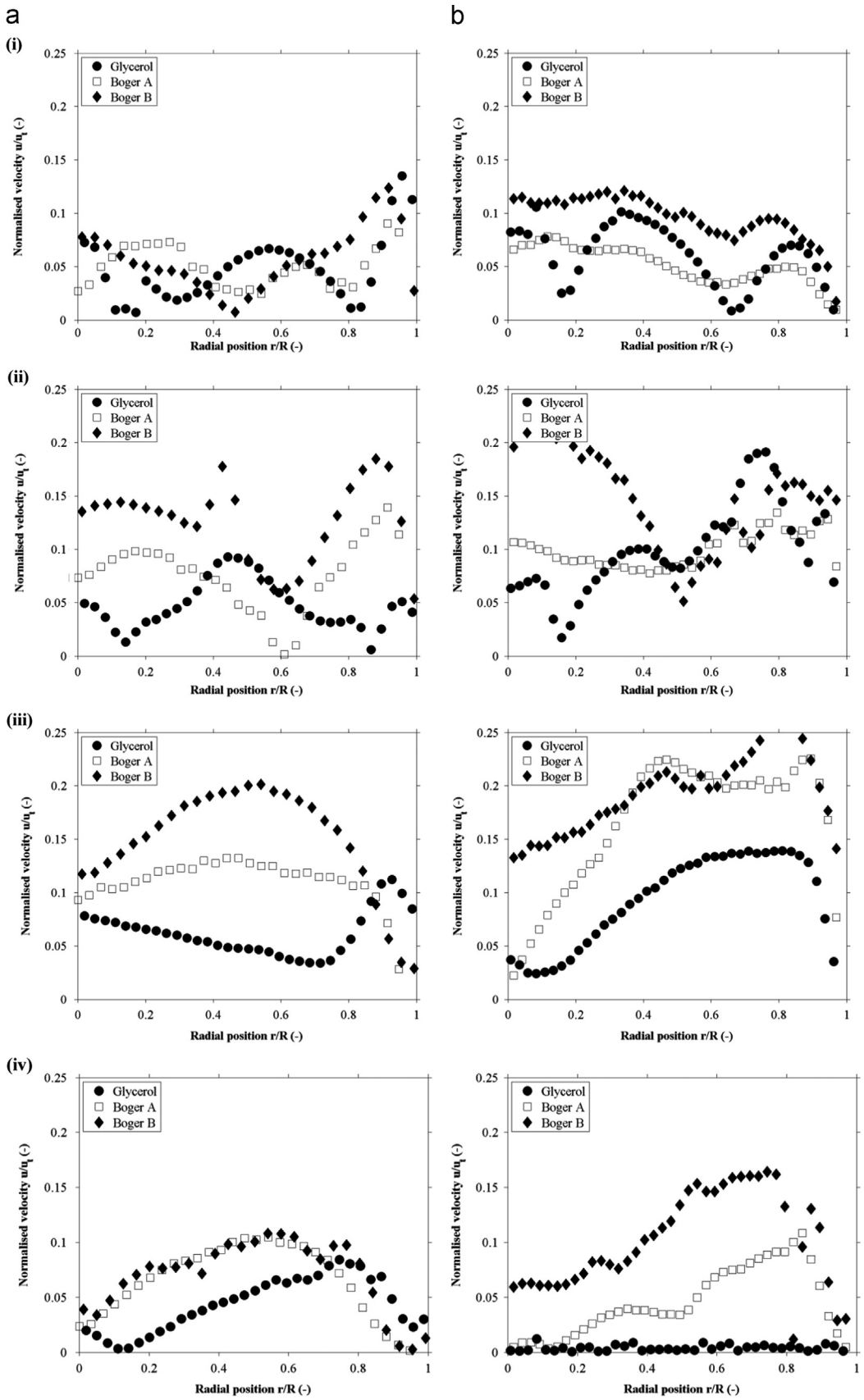

Fig. 10. Normalised velocities at different axial positions; (a) time averaged, (b) angle resolved; (i) $z=C+W/2$, (ii) $z=C$, (iii) $z=C-W/2$, and (iv) $z=0$.

3.2.3. Impeller pumping numbers

Impeller pumping numbers in the axial plane, calculated as described by Eq. (6), are displayed in Table 4.

A small amount of elastic component displays no significant change to the overall impeller pumping capacity. However, as polymer concentration increases there is a significant reduction in impeller pumping capacity as the fluid becomes more elastic. This can be attributed to the increased storage of energy within the fluid, as expected with a viscoelastic medium, compared to the Newtonian equivalent. This reduces the kinetic energy, and thus momentum, transferred to the fluid and therefore lowers the fluid velocity.

As observed in the velocity fields, an increase in the magnitude of fluid elasticity leads to an increase in the ratio of radial to axial pumping number N_{Qr}/N_{Qz}, it appears that the presence of an elastic fluid component drives the flow from a down-pumping axial impeller discharge to a radial pattern. This phenomenon is also observed in the base velocity data, where the flow pattern changes from a single circulation to two radial flow loops. Note that this effect is diminished under the confined flow of D/T ratios of greater than 0.8, as wall effects prevent complete development of purely impeller-governed flow patterns in these geometries. The axial motion reduction can be attributed to the generation of secondary flows within viscoelastic media, generated by normal

Table 4
Impeller pumping numbers N_Q.

Fluid	Impeller rotational speed N (rpm)	Radial pumping number N_{Qr} (dimensionless)	Axial pumping number N_{Qz} (dimensionless)	Total pumping number N_Q (dimensionless)	N_{Qr}/N_{Qz} (dimensionless)
Glycerol	30	0.08	0.16	0.24	0.49
	60	0.09	0.20	0.29	0.45
Boger A	30	0.24	0.06	0.27	4.28
	60	0.22	0.06	0.28	3.68
Boger B	30	0.09	0.02	0.11	5.03
	60	0.15	0.06	0.21	2.46

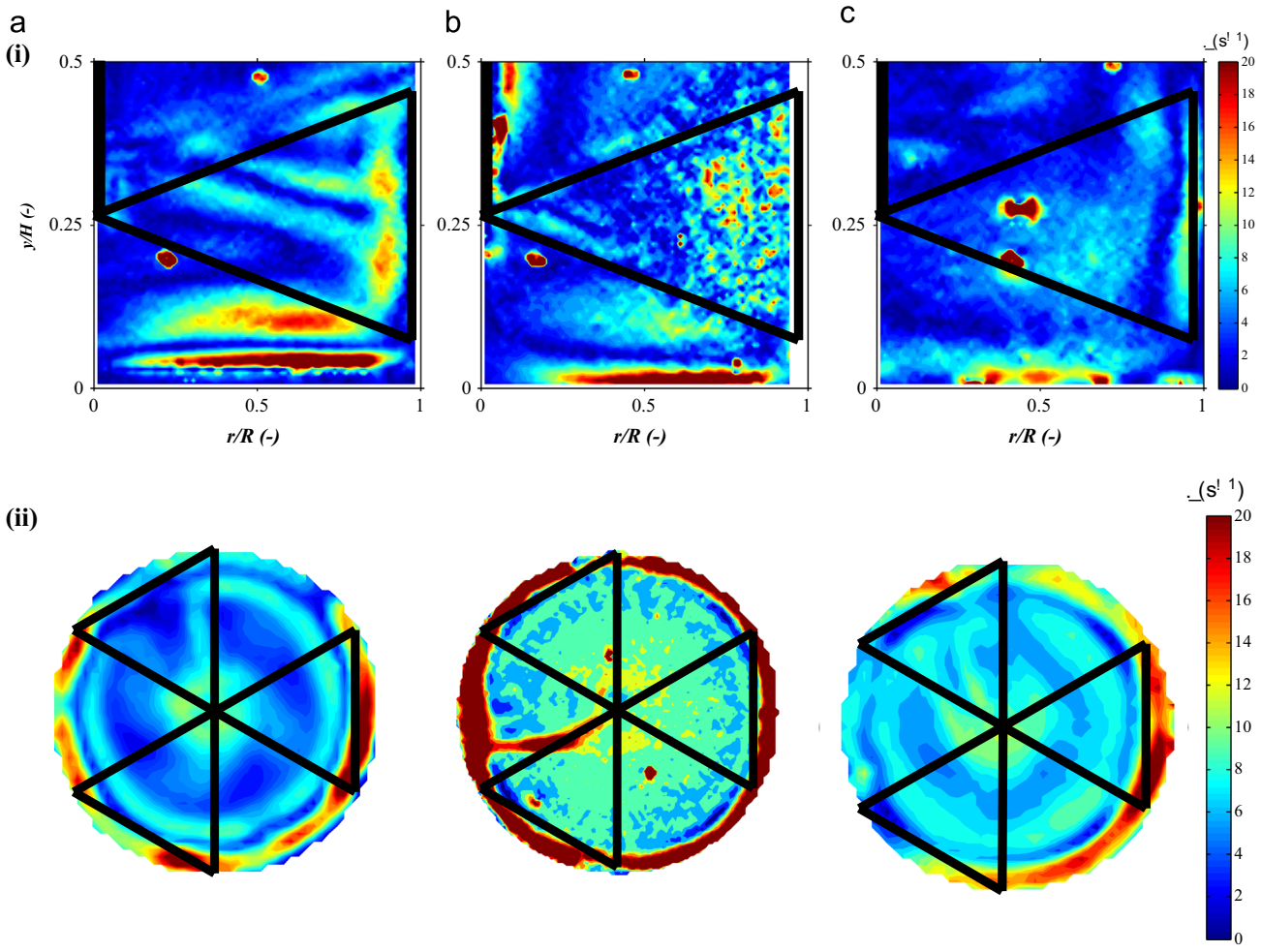

Fig. 11. Local shear rates (time averaged), $D/T=0.98$; (a) Glycerol, (b) Boger A, (c) Boger B; (i) axial plane, (ii) rotational plane, $z=C$.

stresses as the material deforms. These flows act contrary to the principle flow generated by the impeller, causing a reversal of flow element direction, albeit at a significantly lower magnitude than the primary flow. This exhibits itself as a combination effect, creating a shift from axial to radial flow within the impeller. This is expected to have a significant on the mixing performance of viscoelastic media, as a reduction in axial mixing may lead to longer mixing times as the amount of material transfer across the height of the vessel is diminished.

3.2.4. Shear rates

In addition to the velocity fields, it is also necessary to assess the shear performance of the impeller geometries. Of critical importance is the maximum shear rate within the vessel, as this dictates the maximum deformation rate the material is subjected to. Fig. 11 displays the time-averaged shear rate in the axial plane, and the rotational plane at $z=C$ which displays the region of greatest rotational shear rate.

As expected from the velocity fields, shear rates are significantly lower in viscoelastic fluids than the Newtonian equivalent. This is to be expected due to the polymeric material component and the associated decrease in local velocity gradients caused by elastic storage within the material. It can be seen that the greatest deformation occurs around the impeller blades and at the confines of the vessel walls, where flows must change direction quickly causing a large local shear rate. In the rotational plane, shear rates are of an increased magnitude in the radial direction from the vessel centre to the wall, with maxima of approximately 17 s^{-1}, due to solid body rotation and the associated Couette-type flow within the spacing between the impeller blades and the vessel walls. However, away from the impeller clearance significantly lower shear rates are recorded, as solid body rotation limits fluid velocity gradients aside from extensional components, i.e. gradients in the direction of flow. This behaviour indicates that little deformation occurs in the fluid bulk, and thus the principle work of the impeller is imparted to material in the wall clearance.

Predicted k_s values would imply average shear rates in the impeller region of 16 s^{-1} at $N=60$ rpm. Observed shear rates in the rotational plane are however significantly below the expected values and thus local shear rates in the impeller region are lower in practice. In particular it is expected that at D/T values of 0.98 Couette flow would be observed between the impeller blade and the wall, with shear rates expected to be 232 s^{-1}, i.e. $O(10^2)$ s^{-1} according to the equation:

$$\dot{\gamma} \approx \frac{r_1\omega}{r_2-r_1} = \frac{2\pi ND}{T-D} \tag{13}$$

As the maximum shear rates observed are an order of magnitude lower than this value, is likely that true Couette flow does not occur within the impeller clearance. This suggests that the effect of a hollow blade significantly reduces shear rates within the vessel owing to the reduction in flow confinement at the wall. As a possible explanation, it may be that the impeller tip speed is not the most suitable choice of characteristic speed, nor the impeller diameter characteristic of the distance required for calculation of the flow Reynolds number or shear rate in between the impeller and vessel wall. This will in turn affect the determination of impeller performance, as it is expected that Reynolds numbers are currently significantly over-predicted therefore leading to lower impeller effectiveness at a given Reynolds number. A caveat is that this maximum shear rate will only be observed for a very short time as the impeller immediately passes the observation plane. Additionally, the resolution of the velocity field is of the order of the wall clearance (i.e. ~2 mm), and thus may underestimate the

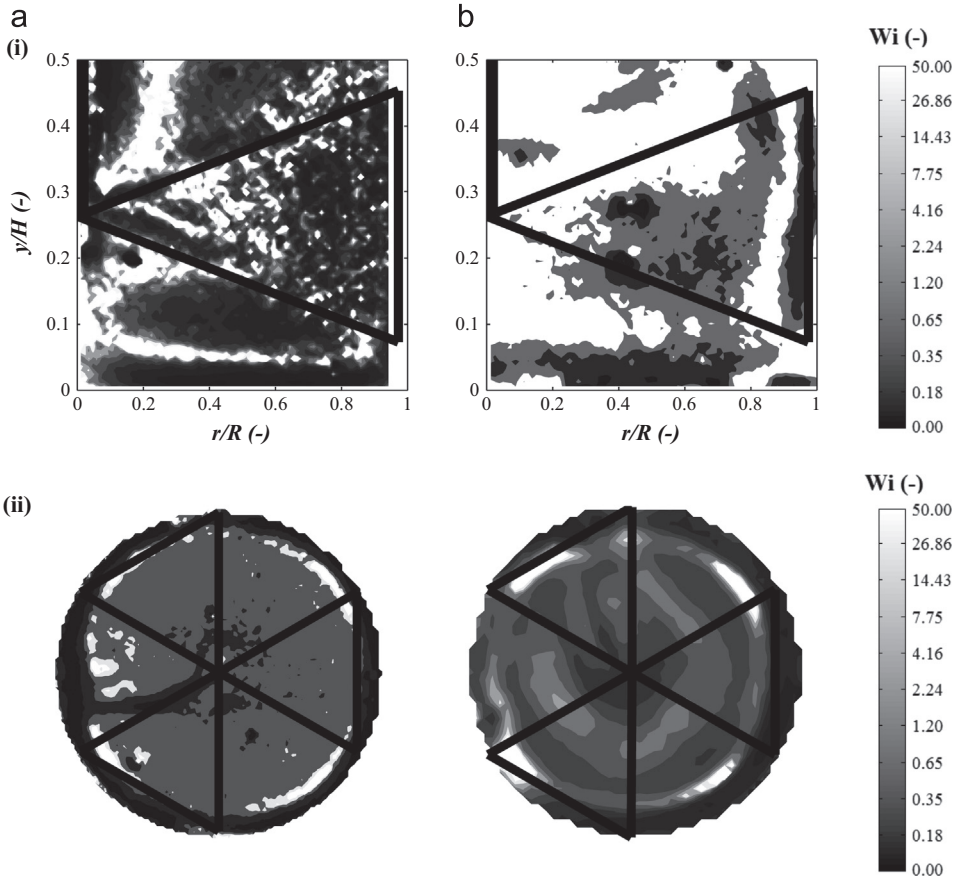

Fig. 12. Local Weissenberg number *Wi* (time averaged), $D/T=0.98$; (a) Boger A, (b) Boger B; (i) axial plane, (ii) rotational plane. *Note: colour scale logarithmic.*

local values of velocity gradient and thus shear rate due to PIV grid resolution.

It should be noted that from the shear rate field, the local elastic effects within a viscoelastic material can be determined through the local Weissenberg number *Wi*. The results of this calculation are shown in Fig. 12.

Owing to the reduction in relaxation time at increasing shear rates, the relation between local shear rate and local Weissenberg number is complex, leading to a disconnection between the location of maximum shear rate and maximum Weissenberg number. However, there is a clear line of maximum Weissenberg number, and thus maximum elasticity, away from the impeller and forming a cavern-like boundary around the fluid. The extent of this cavern couples well with the direction of recorded velocities within the observed flows, indicating that the fluid elasticity is indeed responsible for the formation of pseudo-cavern structures within the geometry. In addition, these lines of maximum *Wi* follow the outermost flow loops observed in the velocity field data, and also the line of the impeller blade cross-section through the image plane.

After having assessed the flow structures and underlying physics of steady-state viscoelastic flows within these vessels, it is now prudent to assess performance in transient systems using a mixing time approach to couple the observed flow effects at all timescales.

3.3. PLIF results

Having assessed steady-state performance, it is necessary to move to a transient system in order to investigate mixing performance over

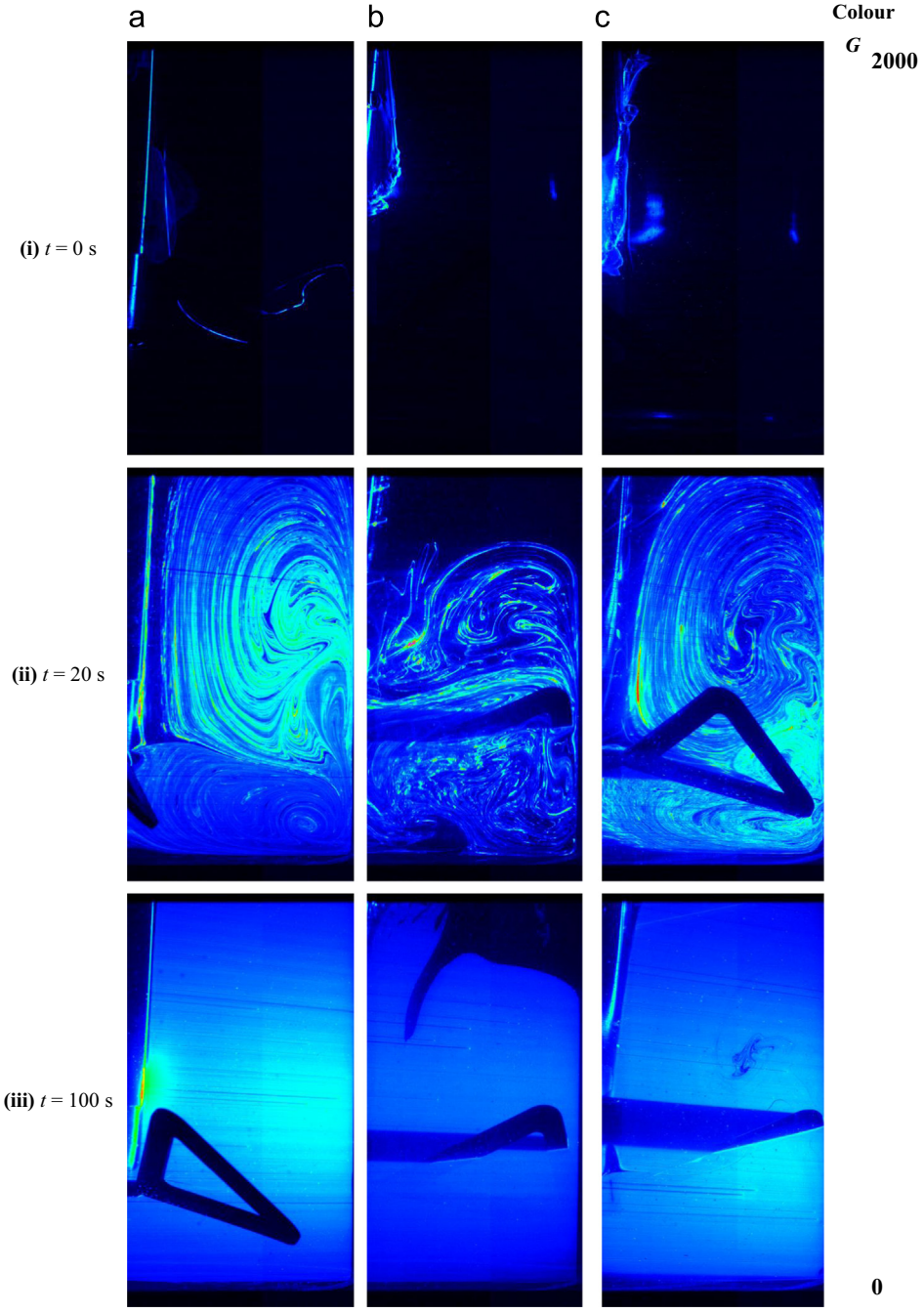

Fig. 13. Development of local concentration over time, $D/T=0.98$, $N=60$ rpm (pseudo-colour); (a) Glycerol, (b) Boger A, (c) Boger B; (i) $t=0$ s, (ii) $t=20$ s, (iii) $t=100$ s.

time. This is achieved using PLIF and calculating mixing times. Mixing performance plots in pseudo-colour plots for the greyscale range $G=0$–2000 are shown in Fig. 13 below.

It can be seen that in the Newtonian fluid, clear striated circulation patterns are visible that follow the streamlines observed in PIV data. The down-pumping flow profile is evident, with several circulations required to produce complete mixing. This is in contrast to the viscoelastic materials, which display a radial pumping flow pattern. However, the highly striated flow nature is common to all rheologies, with the viscoelastic flows both displaying a highly striated flow pattern with stretching patterns clearly seen, indicating an elastic response. In addition, secondary flows caused by normal stress differences are observed close to the impeller shaft, improving the axial mixing performance of the viscoelastic fluid. An unmixed island are also visible immediately above and below the impeller discharge at time $t=100$ s for fluid Boger B, which corresponds with the regions of maximum Weissenberg number (as seen in Fig. 12) within the geometries indicating a solid-like island of limited mixing performance.

Local concentration variance has been assessed to elucidate mixing times, with the logarithm of this value plotted against time in Fig. 14, with final mixing times displayed Table 5. Theoretical mixing times calculated from Eq. (13) are also displayed.

Experimental mixing times show a curious pattern. Although glycerol, the Newtonian comparison, in this case follows the expected 50% reduction mixing time as impeller speed N doubles, the relation does not appear to hold for viscoelastic fluids. In fact, dimensional mixing times $N\theta_{95}$ appear to reduce slightly with an elastic component in the fluid, with this reduction greater at lower elasticities. Further, Boger A shows a four-fold reduction in mixing time as impeller speed doubles, indicating a non-linear relationship. However, further assessment of these fluids highlights some interesting features. The comparison of Elasticity number El with each mixing time condition yields an initial linear trend as shown in Fig. 15, with a steeper gradient for the 95% mixed condition compared to 90%. This suggests that the overall mixing performance is governed by the comparative levels of fluid inertia and elasticity exhibited by the fluid, rather than simply fluid motion or elasticity in isolation. However, it can be seen that for the highest elasticity number, corresponding to fluid Boger B at 30 rpm, the values fall significantly below this linear trend. This may be due to the greyscale values for the fully mixed condition being close to

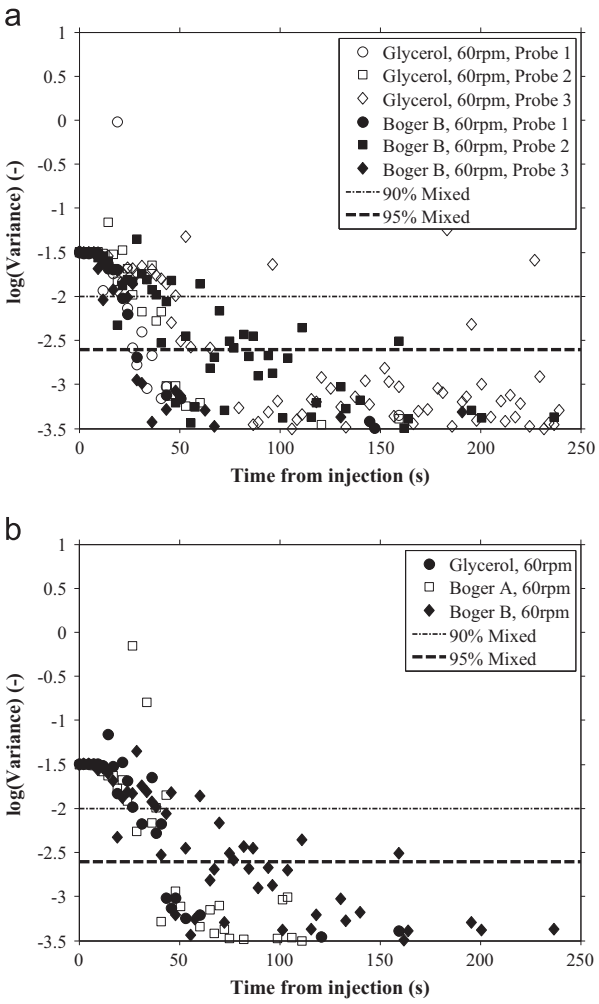

Fig. 14. Concentration variance versus time; (a) Comparison of Newtonian and viscoelastic fluids, (b) Comparison of all fluids at a set probe position.

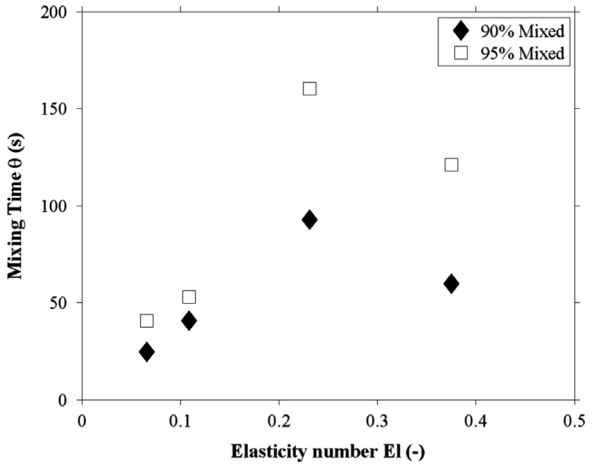

Fig. 15. Comparison of mixing time θ with Elasticity number El.

Table 5
Mixing times.

Fluid	Elasticity number $El=Wi/Re$ (dimensionless)	Impeller rotational speed N (rpm)	Experimental mixing time θ_{90} (s)	Experimental mixing time θ_{95} (s)	Dimensionless mixing time $N\theta_{95}$ (dimensionless)
Glycerol	–	30	96.1	130.0	65.0
	–	60	44.0	55.1	55.1
Boger A	0.231	30	92.8	160.4	80.2
	0.066	60	24.6	40.6	40.6
Boger B	0.375	30	59.9	121.0	60.5
	0.109	60	40.6	53.1	53.1

the background values, thus reducing the reliability of the MATLAB programme in calculating true local concentration variance values in this fluid.

4. Conclusions

The performance of "butterfly" impellers has now been assessed and their interaction with viscoelastic fluids has been observed across a wide range of geometries and experimental conditions. The effect of fluid elasticity was isolated from viscous effects through the use of Boger fluids, which possess constant viscosity of approximately 0.18 Pa s and a measurable elastic response, with fluid relaxation times λ fitting a power law model. From an energy consumption perspective, these impellers perform well compared to other more commonplace geometries such as Rushton disc turbines and down-pumping pitched blade turbines, with the "butterfly" geometry possessing a turbulent Power number *Po* of 0.6 compared to 4.9 for a RDT and 0.8 for a PBTd. Additionally, a value of laminar power gradient K_p of 122 indicates a slightly greater efficiency than a RDT's value of 71. However, despite the improved energy performance, the "butterfly" impeller performs poorly in other areas.

PIV experiments have yielded a wealth of data regarding flow fields and shear rates generated by "butterfly" impellers within Newtonian and viscoelastic fluids. Although impeller pumping numbers N_Q are of a similar magnitude to other geometries, low velocity magnitudes (no more than 25% of the impeller tip speed) in the axial (r–z) plane indicate poor axial mixing performance. Viscoelasticity appears to increase the local velocity magnitudes within the impeller blade hollow whilst causing the flow field to become more uniform, reducing local velocity gradients. Additionally, in the rotational (r–θ) plane velocity magnitudes are maximum 50% of the impeller speed, indicating that the majority of energy input from the impeller goes into purely rotational motion. Further, maximum shear rate magnitudes of 20 s^{-1} indicate poor mixing performance, with fluid elasticity inhibiting shear in the axial plane. Additionally, torque measurements found the Metzner–Otto constant k_s to equal 16, which suggests that shear rates in the impeller region as found by PIV are significantly lower than predicted by the k_s parameter. Maximum shear occurs in the region between the impeller blade and the vessel wall, as expected of close-clearance impeller geometries. However, viscoelasticity appears to reduce shear rates, indicating poor shear performance in the materials that these impellers are designed to work with.

PLIF experiments have yielded apparently conflicting results, with mixing times not appearing to follow the expected trend of decreasing mixing time with increasing impeller rotation rate. However, further analysis of the data shows that fluid Elasticity number *El* is the governing parameter, with increasing values of *El* leading to increased mixing times as fluids exhibit more solid-like behaviour inhibiting mixing. At high values of *El* there appears to be a divergence from this behaviour, which may indicate a change in elastic regime. However, the current data cannot conclusively determine whether this is the case.

Future work with "butterfly" impeller geometries should henceforth focus on fluids with a greater range of elasticity, in particular with regard to the assessment of fluid mixing times in order to determine the presence of differing elastic regimes. Also, the application of novel methods of assessing PLIF images such as the areal mixing distribution should be applied to the stirred tank system to further elucidate the performance of these impellers. Additionally, the assessment of impeller performance with complex multiphase systems would also be highly recommended, as these particular systems are the principal applications of "butterfly" impeller geometries in the process industries.

Nomenclature

Roman letters

a	Power-law pre-exponential factor, s^{b+1}
b	Power-law exponent, dimensionless
C	impeller clearance, mm
C	concentration, g L^{-1}
D	impeller diameter, mm
El	Elasticity number, dimensionless
G	greyscale value, dimensionless
K	Power-law pre-exponential factor, Pa s^n
K_p	laminar Re–Po gradient, dimensionless
k_s	Metzner–Otto constant, dimensionless
M	torque, Nm
n	Power-law exponential factor, dimensionless
N	impeller rotational speed, rpm
N_1	normal stress difference, Pa
N_Q	impeller pumping number, dimensionless
P	impeller power draw, W
Po	impeller Power number, dimensionless
Q	impeller pumping capacity, m^3 s^{-1}
r	local radius, mm
R	vessel radius, mm
Re	fluid Reynolds number, dimensionless
T	impeller tank diameter, mm
u	local velocity magnitude, m s^{-1}
u_t	impeller tip speed, m s^{-1}
v	local velocity, m s^{-1}
W	impeller width, mm
Wi	Weissenberg number, dimensionless
z	axial distance from vessel base, mm

Greek letters

$\dot{\gamma}$	shear rate, s^{-1}
η	fluid apparent viscosity, Pa s
θ_M	mixing time, s
λ	fluid relaxation time, s
μ	fluid Newtonian viscosity, Pa s
ρ	fluid density, kg m^{-3}
σ	variance, dimensionless
τ	shear stress, Pa
ψ	normal stress coefficient, Pa s^{-2}
ω	rotational speed, rad s^{-1}

Subscripts and superscripts

1	first component, dimensionless
2	second component, dimensionless
r	radial direction, dimensionless
z	axial direction, dimensionless
θ	rotational direction, dimensionless

Acknowledgements

John Ramsay is funded by an EPSRC, UK doctoral training grant (EP/K502984/1) from the University Of Birmingham, UK and Johnson Matthey. The authors would like to thank Dr. Tom Rodgers

and Dr. Michael Cooke from the University of Manchester, UK for use of their experimental torque measurement rig.

References

Adams, L.W., Barigou, M., 2007. CFD analysis of caverns and pseudo-caverns developed during mixing of non-Newtonian fluids. Chem. Eng. Res. Des. 85 (A5), 598–604.

Adrian, R.J., 1991. Particle-imaging techniques for experimental fluid-mechanics. Annu. Rev. Fluid Mech. 23, 261–304.

Alberini, F., Simmons, M.J.H., Ingram, A., et al., 2014. Use of an areal distribution of mixing intensity to describe blending of non-Newtonian fluids using PLIF. AIChE J. 60 (1), 332–342.

Bird, R., Stewart, W.E., Lightfoot, E.N., 1960. Transport Phenomena. Wiley, New York, London.

Boger, D.V., Yeow, Y.L., 1992. The impact of ideal elastic liquids in the development of non-Newtonian fluid-mechanics. Exp. Therm. Fluid Sci. 5 (5), 633–640.

Brown, et al., 2004. Handbook of industrial mixing. In: Paul, E.L., Atiemo-Obeng, V.A., Kresta, S.M. (Eds.), Handbook of Industrial Mixing. John Wiley & Sons, pp. p145–p202.

Busciglio, A., Grisafi, F., Scargiali, F., et al., 2014. Mixing dynamics in uncovered unbaffled stirred tanks. Chem. Eng. J. 254, 210–219.

Chhabra, R., Bouvier, L., Delaplace, G., et al., 2007. Determination of mixing times with helical ribbon impeller for non-Newtonian viscous fluids using an advanced imaging method. Chem. Eng. Technol. 30 (12), 1686–1691.

Chung, K.H.K., Simmons, M.J.H., Barigou, M., 2009. Angle-resolved particle image velocimetry measurements of flow and turbulence fields in small-scale stirred vessels of different mixer configurations. Ind. Eng. Chem. Res. 48 (2), 1008–1018.

Fontaine, A., Guntzburger, Y., Bertrand, F., et al., 2013. Experimental investigation of the flow dynamics of rheologically complex fluids in a Maxblend impeller system using PIV. Chem. Eng. Res. Des. 91 (1), 7–17.

Fradette, L., Thome, G., Tanguy, P., et al., 2007. Power and mixing time study involving a Maxblend (R) impeller with viscous Newtonian and non-Newtonian fluids. Chem. Eng. Res. Des. 85 (A11), 1514–1523.

Gabriele, A., Nienow, A.W., Simmons, M.J.H., 2009. Use of angle resolved PIV to estimate local specific energy dissipation rates for up- and down-pumping pitched blade agitators in a stirred tank. Chem. Eng. Sci. 64 (1), 126–143.

Grenville, R.K., Nienow, A.W., 2004. Handbook of industrial mixing. In: Paul, E.L., Atiemo-Obeng, V.A., Kresta, S.M. (Eds.), Handbook of Industrial Mixing. John Wiley & Sons, NY, pp. p507–p542.

Grenville, R.K., Tilton, J.N., 1996. A new theory improves the correlation of blend time data from turbulent jet mixed vessels. Chem. Eng. Res. Des. 74 (A3), 390–396.

Guillard, F., Tragardh, C., Fuchs, L., 2000. A study on the instability of coherent mixing structures in a continuously stirred tank. Chem. Eng. Sci. 55 (23), 5657–5670.

Hall, J.F., 2005. Fluid Mechanics, Mixing & Mass Transfer in High Throughput Experimentation Reactors (Ph.D. thesis). University of Birmingham.

Hall, J.F., Barigou, M., Simmons, M.J.H., et al., 2004. Mixing in unbaffled high-throughput experimentation reactors. Ind. Eng. Chem. Res. 43 (15), 4149–4158.

Hall, J.F., Barigou, M., Simmons, M.J.H., et al., 2005. Comparative study of different mixing strategies in small high throughput experimentation reactors. Chem. Eng. Sci. 60 (8–9), 2355–2368.

Harnby, N., Edwards, M.F., Nienow, A.W., 1992. Mixing in the Process Industries. Butterworth-Heinemann, ISBN 0-7506-3760-9.

Hu, Y.Y., Liu, Z., Yang, J.C., et al., 2010. Study on the reactive mixing process in an unbaffled stirred tank using planar laser-induced fluorescence (PLIF) technique. Chem. Eng. Sci. 65 (15), 4511–4518.

Hu, Y.Y., Wang, W.T., Shao, T., et al., 2012. Visualization of reactive and non-reactive mixing processes in a stirred tank using planar laser induced fluorescence (PLIF) technique. Chem. Eng. Res. Des. 90 (4), 524–533.

Ihejirika, I., Ein-Mozaffari, F., 2007. Using CFD and ultrasonic velocimetry to study the mixing of pseudoplastic fluids with a helical ribbon impeller. Chem. Eng. Technol. 30 (5), 606–614.

Jahangiri, M., 2007. Velocity distribution of helical ribbon impeller in mixing of polymeric liquids in the transition region. Iran. Polym. J. 16 (11), 731–739.

Law, A.W.K., Wang, H.W., 2000. Measurement of mixing processes with combined digital particle image velocimetry and planar laser induced fluorescence. Exp. Therm. Fluid. Sci. 22 (3–4), 213–229.

Lehwald, A., Thevenin, D., Zahringer, K., 2010. Quantifying macro-mixing and micro-mixing in a static mixer using two-tracer laser-induced fluorescence. Exp. Fluids 48 (5), 823–836.

Ozcan-Taskin, N.G., 1993. On the Effects of Viscoelasticity in Stirred Tanks (Ph.D. thesis). University of Birmingham.

Ozcan-Taskin, N.G., Nienow, A.W., 1995. Mixing viscoelastic fluids with axial-flow impellers-flow-fields and power-consumption. Food Bioprod. Process. 73 (C2), 49–56.

Patel, D., Ein-Mozaffari, F., Mehrvar, M., 2014. Tomography images to analyze the deformation of the cavern in the continuous-flow mixing of non-Newtonian fluids. AIChE J. 60 (1), 315–331.

Paul, E.L., Atiemo-Obeng, V.A., Kresta, S.M., 2003. Handbook of Industrial Mixing. John Wiley & Sons, Hoboken, NJ.

Phan-Thien, N., 2002. Understanding Viscoelasticity. Springer, Berlin.

Rodgers, T.L., Cooke, M., Siperstein, F.R., et al., 2009. Mixing and dissolution times for a Cowles disk agitator in large-scale emulsion preparation. Ind. Eng. Chem. Res. 48 (14), 6859–6868.

Seyssiecq, I., Tolofoudye, A., Desplanches, H., et al., 2003. Viscoelastic liquids in stirred vessels-Part I: Power consumption in unaerated vessels. Chem. Eng. Technol. 26 (11), 1155–1165.

Shervin, C.R., Raughley, D.A., Romaszewski, R.A., 1991. Flow visualization scaleup studies for the mixing of viscoelastic fluids. Chem. Eng. Sci. 46 (11), 2867–2873.

Stobiac, V., Fradette, L., Tanguy, P.A., et al., 2014. Pumping characterisation of the maxblend impeller for Newtonian and strongly non-Newtonian fluids. Can. J. Chem. Eng. 92 (4), 729–741.

Stokes, J.R., 1998. Swirling Flow of Viscoelastic Fluids (Ph.D. thesis). University of Melbourne.

Stokes, J.R., Graham, L.J.W., Lawson, N.J., et al., 2001. Swirling flow of viscoelastic fluids. Part 2. Elastic effects. J. Fluid Mech. 429, 117–153.

Szalai, E.S., Arratia, P., Johnson, K., et al., 2004. Mixing analysis in a tank stirred with Ekato Intermig((R)) impellers. Chem. Eng. Sci. 59 (18), 3793–3805.

Weissenberg, K., 1947. A continuum theory of rheological phenomena. Nature 159 (4035), 310–311.

Zadghaffari, R., Moghaddas, J.S., Revstedt, J., 2009. A mixing study in a double-Rushton stirred tank. Comput. Chem. Eng. 33 (7), 1240–1246.

Zhang, M.X., Hu, Y.Y., Wang, W.T., et al., 2013. Intensification of viscous fluid mixing in eccentric stirred tank systems. Chem. Eng. Process. 66, 36–43.